**Table 7 Closed-loop transfer functions for System C**

$$\frac{d}{u_g} = \frac{-0.283(0)(2.0)(15.229)[0.134,2.087]}{(0.028)(2.066)(15.228)[0.445,0.465][0.206,2.039]}$$

$$\frac{d}{w_g} = \frac{-0.75(0.111)(2.0)(15.139)[0.291,1.76]}{(0.028)(2.066)(15.228)[0.445,0.465][0.206,2.039]}$$

$$\frac{d}{d_{\text{command}}} = \frac{-1.426(0.035)(-3.606)(4.396)}{(0.028)(2.066)(15.228)[0.445,0.465][0.206,2.039]}$$

$$\frac{u}{u_g} = \frac{0.0373(0.12)(1.35)(2.169)(15.228)[0.176,1.995]}{(0.028)(2.066)(15.228)[0.445,0.465][0.206,2.039]}$$

$$\frac{u}{w_g} = \frac{-0.136(2.051)(15.224)[-0.17,0.442][0.165,1.96]}{(0.028)(2.066)(15.228)[0.445,0.465][0.206,2.039]}$$

$$\frac{u}{d_{\text{command}}} = \frac{0.194(0)(4.03)(-4.082)}{(0.028)(2.066)(15.228)[0.445,0.465][0.206,2.039]}$$

as preliminary calculations, useful for such things as comparisons between competing systems. Second, the confidence level of the results is a direct function of the confidence level of the gust inputs. But because this information is not currently available, no estimate can yet be made for the confidence level of the computed probabilities.

## Appendix: Summary of Numerical Constants for the Example Systems

This appendix consists of pertinent summary tables taken from Ref. 4. In addition, the longitudinal perturbation equations of motion are given in Eq. (13) for easy reference.

The example aircraft is a DC-8 defined by the landing approach parameters given in Table 4. Table 5 then follows with a list of the various control system constants that were shown in Figs. 3 and 4 (earlier). Finally, the closed-loop system transfer functions used in computing the pertinent rms values are given in Tables 6 and 7.

$$\begin{bmatrix} s - X_u & -X_w & g\cos\Theta_0 \\ -Z_u & s - Z_w & -U_0 s + g\sin\Theta_0 \\ -M_u & -(M_{\dot{w}}s + M_w) & s(s - M_q) \end{bmatrix} \begin{bmatrix} u \\ w \\ \theta \end{bmatrix} = \begin{bmatrix} X_{\delta_e} \\ Z_{\delta_e} \\ M_{\delta_e} \end{bmatrix} \delta_e \quad (13)$$

$$\dot{h} = -U_0\sin\Theta_0 - w\cos\Theta_0 + u\sin\Theta_0 + U_0\cos\Theta_0\theta$$

## References


[1] Wood, K. A., "The Calculation of Weather Minima—Part I, RVR Minima," *All-Weather Operations Panel, Third Meeting, Vol. II, Selected Working Papers*, International Civil Aviation Organization Doc. 8685, AWOP/III-2, 1967, pp. 167–185.

[2] Chalk, C. R., T. P. Neal, T. M. Harris, F. E. Pritchard, and R. J. Woodcock, *Background Information and User Guide for MIL-F-8785B(ASG)*, "Military Specification—Flying Qualities of Piloted Airplanes," AFFDL-TR-69-72, Aug. 1969, Wright-Patterson Air Force Base, Ohio.

[3] Criteria for Approval of Category II Landing Weather Minima, FAA AC 120-20, June 6, 1966.

[4] Johnson, W. A., and D. T. McRuer, *Development of a Category II Approach System Model*, TR 182-3, Nov. 1970, Systems Technology, Inc., Hawthorne, Calif.


DECEMBER 1971 J. AIRCRAFT VOL. 8, NO. 12

# Prediction of Installed Nozzle Flowfields


W. Presz Jr.,* M. Konarski,† and E. Grund‡

*Pratt & Whitney Aircraft, East Hartford, Conn.*



**Spreiter and Alksne's method of local linearization was improved and used for inviscid-transonic-flow calculations over axisymmetric bodies of revolution (equivalent bodies). This solution was iteratively coupled with a boundary-layer inner solution allowing it to be used over bodies with slight slope discontinuities. The results of applying this method to simple axisymmetric fuselages and afterbody shapes are compared with experiments. For nonaxisymmetric bodies, cross-flow corrections are derived from incompressible flow theory and are coupled with the equivalent body results to approximate the complete transonic flowfield. The analysis is shown to be useful for supplementing test data and predicting installed nozzle performance.**


## Introduction

ONE of the most complex and demanding problems during the design of new aircraft is the proper integration of the propulsion system into the airplane structure. Here the aircraft/nozzle interface is of special importance, since the external flowfield set up by the vehicle exerts control over the aft-end flow, and hence, external pressure environment of the exhaust system. As a result, the thrust-minus-drag characteristics of the nozzle may change substantially and significantly affect vehicle performance. In addition, certain nozzle types (plug nozzles, blow-in-door ejectors) experience beneficial interactions between the external and internal flowfields to broaden the range of efficient nozzle operating conditions. In these cases, information about the flowfield external to the nozzle is even more critical.

Information on these interactions or installation effects is generated primarily by airframe/nozzle models in a wind tunnel. Wind-tunnel test data, however, are usually confined to measurements of gross aft-end forces to speed data recording and thereby, minimize the occupancy time required for these costly experiments. At best, only small amounts of pressure distribution data are measured making evaluation of


Presented as Paper 70-700 at the AIAA 6th Propulsion Joint Specialist Conference, San Diego, Calif., June 15–19, 1970; submitted July 16, 1970; revision received May 28, 1971.



* Senior Analytical Engineer, Inlets & Nozzles Group, Advanced Gas Turbines. Associate Member AIAA.

† Assistant Project Engineer, Inlets & Nozzles Group, Advanced Gas Turbines.

‡ Project Engineer, Inlets & Nozzles Group, Advanced Gas Turbines. Associate Member AIAA.

results difficult and providing little insight into the actual nature of the interacting flowfields. The effects of additional factors such as model support interference and model inlet compromises become all the more difficult to assess, particularly at transonic Mach numbers where they are most pronounced.

An analytic method which will calculate pressure distributions over the airframe and nozzle sections will, therefore, offer several advantages including; 1) an early assessment of airframe/nozzle installation effects, 2) better understanding of external/internal flowfield interactions, and 3) more efficiently designed wind-tunnel experiments for improved test data by correcting the model compromises and support interferences.

This paper presents such an analytical approach. Since accurate numerical solutions to the problem of flow prediction around both axisymmetric and three-dimensional bodies are available for moderate and high-supersonic speeds as well as at subsonic Mach numbers, the method concentrates on the transonic speed range. Specifically, a procedure is outlined for calculating the external aerodynamic characteristics of a three-dimensional body traveling at transonic Mach numbers. Analytical results are compared with experimental data to demonstrate that the theoretical approach produces good estimates of afterbody pressure fields. Examination of the component theories contributing to the three-dimensional analysis leads up to and culminates in the comparison of predicted surface pressures with test data for a realistic typical twin jet fighter. This comparison proves the validity of the theoretical approach and shows that good estimates of installed exhaust system performance can be obtained for complex aircraft/nozzle geometries.

## Development of Analysis

Starting point of the analysis is Spreiter and Alksne's method of solving the nonlinear transonic-flow equation.[1] The transonic potential flow equation in its small perturbation form is written for an axisymmetric body as

$$[1 - M_\infty^2 - M_\infty^2(\gamma + 1/U_\infty)\varphi_x]\varphi_{xx} + (1/r)\varphi_r + \varphi_{rr} = 0 \quad (1)$$

Here, $U_\infty$ designates the freestream velocity, $M_\infty$ the corresponding Mach number and $\gamma$ the ratio of specific heats; $\varphi$ represents the perturbative velocity potential, whereas, $x$ and $r$ are axial and radial coordinates, respectively. This equation, together with appropriate boundary conditions, must be solved to arrive at a description of the flowfield surrounding a body of revolution at transonic speed. For the case of subsonic approach speeds, Spreiter and Alksne rewrite Eq. (1) in the form

$$\lambda\varphi_{xx} + (1/r)\varphi_r + \varphi_{rr} = 0 \quad (2)$$

and assume that the variation in $\lambda$ is small so that it can temporarily be considered constant. Then the problem reduces to one familiar from linearized subsonic flow theory and the solution can be stated as

$$\varphi = -\frac{U_\infty}{4\pi}\int_0^l \frac{S'(\xi)d\xi}{[(x-\xi)^2 + \lambda r^2]^{1/2}} \quad (3)$$

where $l$ is the body length and $S(x)$ represents its cross-sectional area curve. The perturbative velocity distribution on the surface of a slender and smooth body follows by differentiation. The result, after some simplifying approximations becomes

$$u/U_\infty = [S''(x)/4\pi]\ln\lambda + u_i/U_\infty \quad (4)$$

where

$$\frac{u_i}{U_\infty} = \frac{S''(x)}{4\pi}\ln\frac{S(x)}{4\pi x(l-x)} + \frac{1}{4\pi}\int_0^l \frac{S''(x) - S''(\xi)}{|x-\xi|}d\xi \quad (5)$$

$u$ signifies the local compressible perturbation velocity on the body surface in the $x$ direction and $u_i$ its counterpart at $M_\infty = 0$. Differentiating expression, Eq. (4), and restoring the original quantity represented by $\lambda$ results in

$$\frac{d}{dx}\left(\frac{u}{U_\infty}\right) = \frac{S'''(x)}{4\pi}\ln\left[1 - M_\infty^2 - M_\infty^2 \times \frac{\gamma+1}{U_\infty}u\right] + \frac{d}{dx}\left(\frac{u_i}{U_\infty}\right) \quad (6)$$

Equation (6) describes the compressible perturbation velocity distribution $u$ in the axial direction on the body surface. The equation is of first order, ordinary and nonlinear, and can be solved by any of a number of numerical methods. The constant of integration for Eq. (6) is determined by assuming that $u = u_i$ at the point on the forebody where $S''(x) = 0$ as suggested by Eq. (4).

For complex bodies with nonanalytic cross-sectional area distributions, the incompressible velocity distribution, Eq. (5), of Spreiter and Alksne produces singularities and is numerically difficult to calculate. Also, under these conditions the incompressible calculated velocity distribution does not always agree favorably with experimental results. This portion of the analysis was therefore modified by introducing for $u_i$ an expression based on slender body theory without Spreiter and Alksne's simplifying assumptions. When the perturbative velocity potential $\varphi$, Eq. (3), is written in its incompressible form by setting $\lambda = 1$, the following equation is derived by differentiation with respect to the axial coordinate

$$\frac{u_i}{U_\infty} = +\frac{1}{8\pi}\int_0^l S'(\xi)\frac{2(x-\xi) + S'(x)/\pi}{[(x-\xi)^2 + S(x)/\pi]^{3/2}}d\xi \quad (7)$$

Not only are some of the assumptions in the derivation of Eq. (5) eliminated, but the equation also has better numerical stability characteristics since only first derivatives of the area distribution curve appear.

An analogous analysis applies to the case of supersonic freestream Mach numbers and a somewhat different approach yields similar expressions for $M_\infty = 1$. Details can be found in Ref. 1.

An investigation shows that for Mach numbers from about 1.0 to 1.1, the transonic-flow solution for axisymmetric fuselages developed by Oswatitsch and Keune[2] resulted in better agreement with experimental data than the supersonic local linearization method. Characteristically, instead of linearizing the transonic-flow equation, Eq. (1), by regarding the part $1 - M_\infty^2 - M_\infty^2(\gamma + 1/U_\infty)\varphi_x$ of the nonlinear term temporarily as constant, as is done in Spreiter and Alksne's analysis, Oswatitsch assumes constancy of the other part, i.e., $M_\infty^2(\gamma + 1/U_\infty)\varphi_x$ and then proceeds to solve the resulting linear differential equation. Particulars of the analysis as applied to afterbodies can be found in Ref. 3. Hence, different equations, some originally derived by Spreiter and Alksne and some by Oswatitsch and Keune, are used to describe regions of locally subsonic, transonic and supersonic flows. Without going into detail, it is noted that these different flow solutions are patched together at appropriate axial locations. Recompression of any locally supersonic flow to subsonic speeds is effected by means of shock wave. The present analysis provides for the inclusion of a shock wave in the patching process, its strength and location being determined from empirical correlations. A detailed discussion of the patching process including the incorporation of the shock wave is presented in Ref. 3.

The modified version of Spreiter and Alksne's method of local linearization and Oswatitsch's solution have been used to calculate flow characteristics on the surface of axisymmetric bodies for subsonic and supersonic approach Mach numbers. The methods as outlined form one building block for calculating three-dimensional transonic flows.

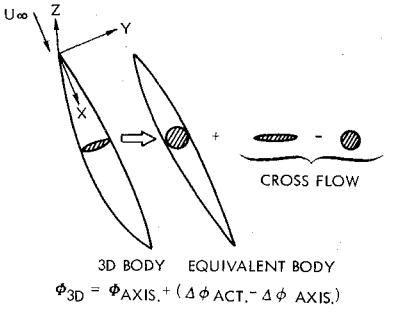


**Fig. 1 Buildup of 3D transonic flow.**

A compressible turbulent boundary-layer calculation routine was coupled with the inviscid analysis to approximately account for viscous effects on the flowfield surrounding the body under consideration. This was done by adding the displacement thickness $\delta^*$, obtained from a modified Reshotko-Tucker boundary-layer analysis[4] to the basic body shape; the inviscid-transonic flowfield is then calculated over this slightly thicker configuration. Since $\delta^*$ is affected by the pressure distribution impressed on the boundary layer by the external flowfield, the inclusion of the boundary-layer effects into the analysis has to be done iteratively; a displacement thickness is determined and added to the cross-sectional area distribution. This augmented area is then used to predict the flowfield including the pressure distribution along the body. The pressures in turn define a new $\delta^*$ variation which is added to the area distribution in place of the previous one and the cycle is repeated until convergence is obtained. Because the approximations made in the derivation of the inviscid analysis, a more detailed and exact boundary-layer calculation than the one used is not called for.

An additional benefit was, however, derived from the inclusion of this first-order viscous analysis. The inviscid theory as presented is not capable of handling surface discontinuities since the assumptions made in the derivation require smooth contours, i.e., continuous first and second derivatives of the area distribution curve. Addition of the boundary-layer displacement thickness to the body contour eliminates slight surface discontinuities and results in a boundary-layer/external flow interface which will be smooth to at least the second derivative in $S(x)$. Thus, the boundary-layer routine helps to eliminate possible numerical instabilities in the flowfield calculation.

The transonic equivalent body analysis which forms the basis of the theoretical approach presented here, is supplemented by three-dimensional potential flow theory to account for nonaxisymmetric velocity and pressure components in the flowfield. This is done by superimposing on the axisymmetric compressible flowfield an incremental velocity distribution acting in planes perpendicular to the axial direction.

One of the basic results of slender body theory which forms a fundamental ingredient of this analysis states that the flow in a plane normal to the body longitudinal axis can be treated independently of the flow in the axial direction. Also, the flow in the cross-flow plane is independent of approach Mach number and hence can be treated incompressibly. In practice, the incremental velocities due to nonaxisymmetry of a body are calculated by considering differences in the incompressible flowfield at corresponding points on the three-dimensional configuration and its equivalent body of revolution. Laplace's equation is solved for both cases subject to the boundary conditions of zero normal velocity at the body surface and vanishing flow disturbance far from the body.

The results of axisymmetric transonic analysis, potential flow theory, and boundary-layer-analysis can now be combined to describe the complete flowfield about three-dimensional slender bodies at transonic approach speeds. The process can best be illustrated by referring to Fig. 1. On the left is a schematic of a nonaxisymmetric configuration to be investigated. The flowfield surrounding this body is built up from the transonic flow solution around the equivalent body of revolution, plus an incompressible cross-flow correction arising as the difference in flow velocities between the three-dimensional and the axisymmetric bodies.

In adapting this procedure to a digital computer, the input, i.e., the cartesian coordinates describing the body geometric shape, are first used to generate the cross-sectional area distribution and the equivalent body of revolution. Subsequently, the transonic flowfield is calculated over the equivalent body as well as the incompressible flow over both the three-dimensional and the equivalent body. Then the cross-flow velocities are obtained as discussed and finally are combined with the transonic solution to provide a complete flowfield description over the nonaxisymmetric configuration at transonic Mach numbers.

The Appendix presents a derivation and a theoretical justification for the approach outlined in this section. Using the concept of inner and outer flow solutions and patching these solutions at an appropriate distance away from the body it is shown that the velocity potential over an arbitrary three-dimensional slender body is equal to the potential of the equivalent axisymmetric body plus a cross-flow potential which is independent of Mach number. In the derivations use has been made of Refs. 5 and 6.

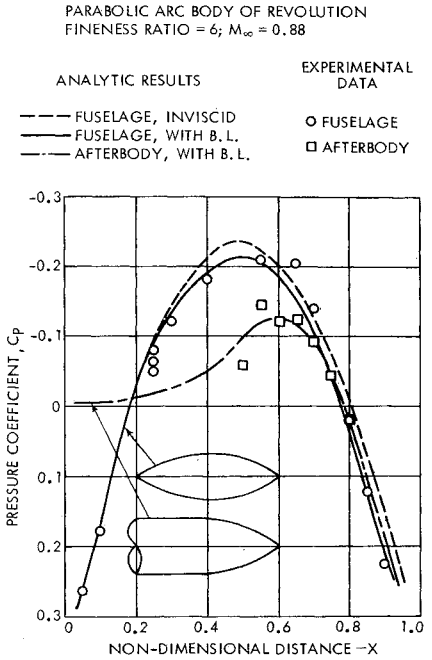


**Fig. 2 Comparison analysis-experiment.**

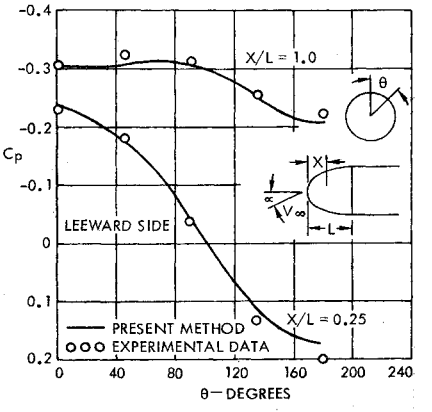


**Fig. 3 Circumferential pressures on ellipsoid-cylinder.**

## Comparison of Analysis and Experiment

The separate components used to build up the three-dimensional transonic flow analysis were compared extensively to experimental data to establish the validity of the theoretical approach. A sample of these comparisons, as well as experimental verification of the independence of cross-flow terms with Mach number, will be presented in this section.

Spreiter and Alksne's nonlinear transonic-flow solution for axisymmetric bodies applies to two different types of body shapes: a closed body representing a fuselage, and an open ended body representative of an aircraft aft end. Figure 2 shows a comparison of analytical results and experimental data for both fuselage and afterbody shapes. Both configurations are parabolic arc bodies of revolution with the afterbody being the aft end of the fuselage mounted on a forward sting. The fuselage has a fineness ratio of 6 and thus is within slender body assumptions. The approach Mach number of 0.88 produces a flowfield which is transonic with sizable compressibility effects. The agreement with data is excellent for both bodies. The two analytic curves for the fuselage represent the inviscid pressure distribution over the body and the more complete solution accounting for boundary-layer effects through a displacement thickness correction. It is apparent that the boundary layer plays an important part in determining pressures on the aft end of the fuselage. The extent and strength of the expansion region is decreased by the boundary layer. This effect is well accounted for when using the Reshotko-Tucker boundary-layer analysis.

Three-dimensional potential flow solutions are obtained by solving Laplace's equation subject to the conditions of vanishing flow disturbance far from the body and of zero normal velocity at the body surface. This latter condition is met by distributing a large number of point sources and sinks over the body surface and adjusting their strength until velocity components normal to the body at its surface vanish. Figure 3 shows a comparison of measured and calculated circumferential pressure distributions at two axial stations for an ellipsoid cylinder combination. The body is inclined about 6° relative to the freestream. The experimental data points are compared to results of the present numerical solution; agreement is excellent attesting to the utility of the method used.

Analytical models are generated by specifying points in a three-dimensional coordinate system to describe the body surface. In adapting the potential flow calculation to a digital computer, preparation of correct input describing the configuration geometry to the machine becomes a major problem. Because the large number of points necessary to trace the body accurately, errors are inevitable resulting in wasted effort and computer time and in a lengthy checkout process. To speed up the checkout operation, computer graphics methods are used extensively. The body under consideration can be viewed on the display terminal from different directions, rotated and magnified. Errors can be spotted easily and corrected, and the corrections recorded in the computer.

Three-dimensional potential flow theory was used to generate the cross-flow pressure corrections over the nonaxisymmetric quadripole body represented schematically in Fig. 4.

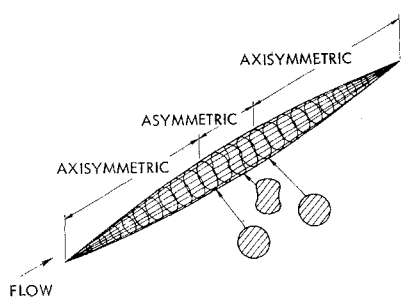


**Fig. 4 Isometric view of quadripole body.**

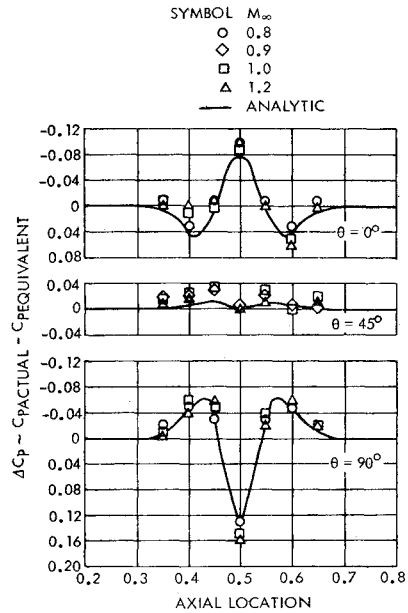


**Fig. 5 Mach number independence of cross-flow.**

This body has a fineness ratio of 14 and an area distribution equal to that of a corresponding parabolic arc body of revolution. The general characteristics of this configuration are well within the slender body assumptions and permit good predictions of equivalent body pressure distributions. Although only 20% of the body length is not axisymmetric, the noncircular section produces major local disturbances which vary circumferentially. Since extensive test results for this body were available, a check on the analytical prediction of cross-flow effects can be made. Figure 5 presents the difference in pressure coefficient between equivalent body and three-dimensional configuration, representing the cross-flow pressure corrections due to the noncircular cross sections. These cross-flow terms were obtained neglecting viscous effects. Agreement between the analytic prediction and experimental data in general is good. Test data scatter is random and justifies the general conclusion that the cross-flow pressure coefficient is independent of Mach number for the body under consideration. The three separate curves in the figure show surface pressure variations in the axial direction at different circumferential locations. These analytically derived cross-flow pressure coefficients were coupled with the equivalent body analytical results for Mach numbers of 0.9, 1.0, and 1.2 to produce the composite pressure coefficients shown in Figs. 6 and 7. The good agreement between the experimental and analytical results is an indication that the approximate theory can be used to produce useful data trends for three-dimensional slender bodies.

In the foregoing paragraphs, the analytic method was applied to simple slender fuselages that fall within the assumptions of the theory. Applications are now presented which typify the usefulness of the analysis for practical and more complex bodies.

The first is a strut supported wind-tunnel exhaust nozzle model that was tested by NASA at the Langley Research Center. Its analytical counterpart is shown isometrically in Fig. 8. The basic model is an axisymmetric fuselage that consists of an ogive nose, cylindrical midsection and a boattailed aft end. Exhaust jets were simulated in the test program by pressurized air. Two support struts are attached to the fuselage midsection. The struts were swept 45° and consisted of NACA 65-0010 profiles. For the analysis, the fuselage, struts and exhaust jet were described to the computer in the form shown in Fig. 8. Cylindrical exhaust jet sections were used to represent a nozzle pressure ratio of 2.

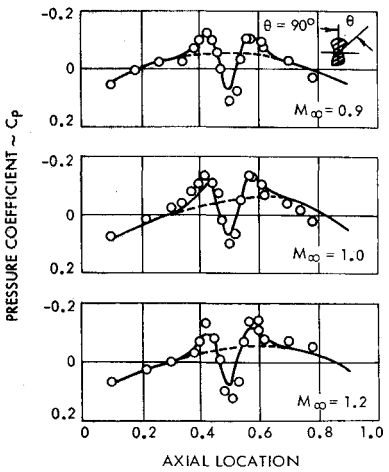


**Fig. 6 Pressure distribution over quadripole body.**

The analytically derived pressure distributions for the test configurations are compared with test results in Fig. 9. Pressures were measured along the fuselage surface in a 45° radial plane. In the figure, three analytically derived pressure variations are presented. The isolated body represents pressures obtained by analyzing the axisymmetric fuselage body without support struts (i.e., no strut interference). The strut mounted body curve reflects pressures derived with the three-dimensional analysis for the complete fuselage and strut assembly. The equivalent body curve shows pressures determined from an equivalent axisymmetric body having the same area distribution as the complete fuselage and strut combination.

From the comparison, it is apparent that the analytic results are in reasonable agreement with experimental data. The body treated herein has dimensions normal to the freestream that are of the same order of magnitude as the body length. To obtain the cross-flow terms, all boundary-layer effects were neglected. Thus, if any separation or high boundary layer to body thickness ratio regions exist the method will be in error. Even with these restrictions and the errors associated with them, the present analysis produces good results. It is therefore concluded that the equivalent body theory coupled with cross-flow corrections can be applied at transonic Mach numbers with reasonable success giving a first-order estimate of wind-tunnel support strut interference.

The analytic procedure can be extended to more complex nozzle installations such as the one on a typical twin-jet fighter shown in Fig. 10. Only one half of the actual aircraft was programed to reduce necessary computer storage and calculation time. For this study, the inlet stream tube as well as the nozzle exhaust plume were simulated by solid surfaces. The transonic flow solution was used to obtain preliminary estimates of asymmetric loads over the nozzle section. The top of Fig. 11 shows the starboard half of a typical aircraft cross section near the nozzle exit. For the various circumferential angles indicated on the sketch, the main part of the figure compares predicted and measured aft end pressure distributions in the axial direction. The calculations were terminated at the axial station of the nozzle exit plane; the freestream Mach number was 0.8 with the vehicle at zero angle of attack.

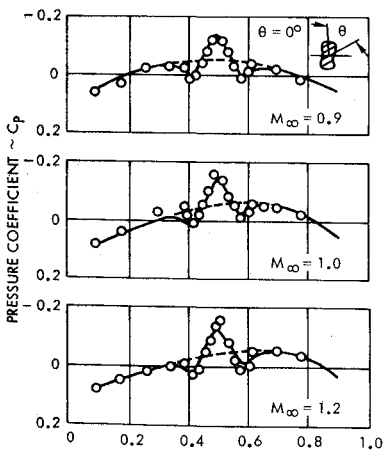


**Fig. 7 Pressure distribution over quadripole body.**

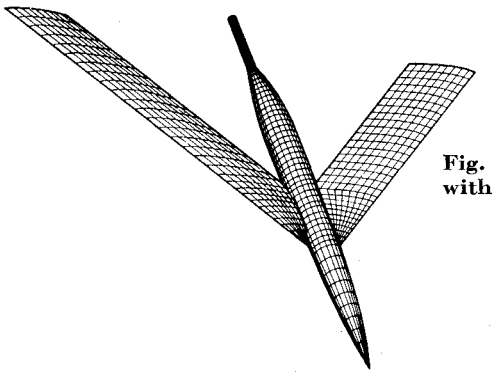

**Fig. 8 Test body with support struts.**

Considering that the effects of wake and corner flows were neglected, the general agreement is good. Therefore, even for complex twinjet bodies the three-dimensional analysis is capable of providing reasonable engineering estimates of external flow properties.

## Conclusions

The analysis outlined in this paper is subject to several restrictions. Among them are the assumptions of slender body theory, and the inability to account for lift and regions of separated flow.

The first assumption is not considered critical because most practical aircraft shapes fall into the slender body regime. It is felt that failure to account for lift in the analysis compromises results at angle of attack. Therefore, the capability to treat lifting flowfields is at present being added to the theory. The prediction of separated flow regions and their accommodation within the framework of this approach is unresolved at the present time and more work is needed.

In summary, the examples presented in the previous section support the conclusion that this analysis is a valuable tool for predicting the three-dimensional flowfield surrounding aircraft configurations and its applicable to airplane aft end/nozzle combinations. The theory, with the aforementioned restrictions, gives valid results in the transonic-flow regime for Mach numbers ranging from about 0.7 to 1.2.

## Appendix

The velocity potential over a three-dimensional slender body will be related to the flow over the corresponding equiva-

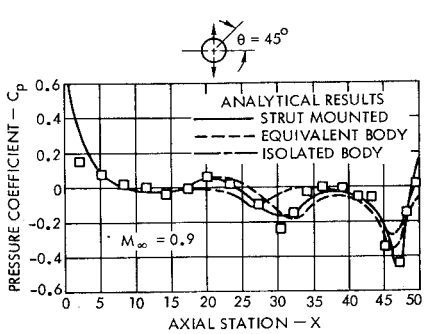


**Fig. 9 Pressure distributions over strutted body.**

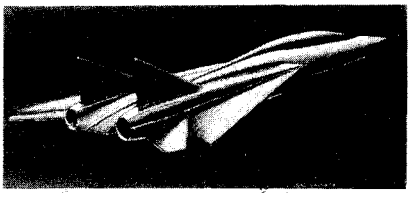

**Fig. 10 Typical twinjet configuration.**

lent body, and a cross-flow term which is independent of Mach number.

In terms of a velocity potential $\phi$, sound velocity $a$, and freestream velocity $U_\infty$, the exact governing equation for steady, adiabatic, irrotational flow is

$$(\phi_x^2 - a^2)\phi_{xx} + (\phi_y^2 - a^2)\phi_{yy} + (\phi_z^2 - a^2)\phi_{zz} + (\phi_{xy} + \phi_{yx})\phi_x\phi_y + (\phi_{yz} + \phi_{zy})\phi_y\phi_z + (\phi_{zx} + \phi_{xz})\phi_z\phi_x = 0 \quad \text{(A1)}$$

where

$$a^2 = a_\infty^2 + [(\gamma - 1)/2](\phi_x^2 + \phi_y^2 + \phi_z^2 - U_\infty^2)$$

A generalized function can be used to represent an arbitrary three-dimensional slender body as follows

$$B(x,y,z) = 0 \quad \text{(A2)}$$

The solution of Eq. (A1) coupled with the boundary conditions associated with Eq. (A2) will have the dominating characteristic that it is a function of the body's thickness ratio. Furthermore, in the limit of very small thickness ratios, one or more of the derivative terms will become negligible. This is a classical warning of singular behavior of the differential equation. In a straightforward perturbation scheme, these derivatives are lost in the first few approximations so that the order, or nonlinearity of the equation is underestimated. One or more boundary conditions must be abandoned, and the approximation breaks down near where they were to be imposed.

To avoid these problems in solving Eq. (A1) for slender bodies, the method of matched asymptotic expansions[5] was used. This method is applied by dividing the flowfield into the two regimes as shown in the following Fig. 12.

Solutions are approximated in each regime by an asymptotic series. The inner and outer solutions are matched in an overlap domain where the inner solution series, taken in the limit of large values of the independent variables, agrees with the outer series solution taken in the limit of vanishing independent variables. This matching procedure allows boundary conditions at the body surface and freestream to be satisfied without over simplifying important flow characteristics normally associated with an asymptotic series solution.

Arguments justifying the method of matched asymptotic expansions, as well as showing that $(\phi^i)_{AB} - (\phi^i)_{EB}$ is independent of Mach number, can now be formulated. The superscript $i$ signifies the inner solution, the subscripts $AB$ and $EB$ refer to the actual and the equivalent body, respectively. The inner regime solution $\phi^i$ is obtained by assuming a power series solution in terms of the thickness parameter $\epsilon$. As the thickness parameter is decreased, the transverse coordinates $y$ and $z$ of the body diminish and reduce the flowfield perturbations in the cross-flow plane. Within the inner regime, the flowfield is stretched in the transverse direction near the body so that the flow properties are not lost as the thickness ratio becomes small. The perturbation potentials become functions of $x$ and the stretched coordinate variables $y$ and $z$ (i.e., $\bar{y} = y/\epsilon$ and $\bar{z} = z/\epsilon$).

The assumed inner series solution is

$$\phi^i = U_\infty[x + \epsilon\varphi_1{}^i(x,\bar{y},\bar{z}) + \epsilon^2\varphi_2{}^i(x,\bar{y},\bar{z}) + 0(\epsilon^3)] \quad \text{(A3)}$$

The assumed outer regime solution is similar except the perturbation potentials are written in terms of the actual variables $y$ and $z$

$$\phi^0 = U_\infty[x + \epsilon\varphi_1{}^0(x,y,z) + \epsilon^2\varphi_2{}^0(x,y,z) + 0(\epsilon^3)] \quad \text{(A4)}$$

Considering first the inner-flow regime, $\varphi_1{}^i$, must be a function of $x$ only; otherwise, the velocity components perpendicular to the body axis would not vanish in the limiting case of zero thickness. Using this result and substituting Eq. (A3) into Eq. (A1) and dropping all higher order terms, Eq. (A5) is obtained

$$\varphi_{2\bar{y}\bar{y}}{}^i + \varphi_{2\bar{z}\bar{z}}{}^i = 0 \quad \text{(A5)}$$

Applying the boundary condition that the normal velocity at the body surface has to be zero gives

$$\nabla B \cdot \nabla\phi^i = 0 \quad \text{(A6)}$$

and after expansion to the proper order

$$B_x + B_{\bar{y}}\varphi_{2\bar{y}}{}^i + B_{\bar{z}}\varphi_{2\bar{z}}{}^i = 0 \quad \text{(A7)}$$

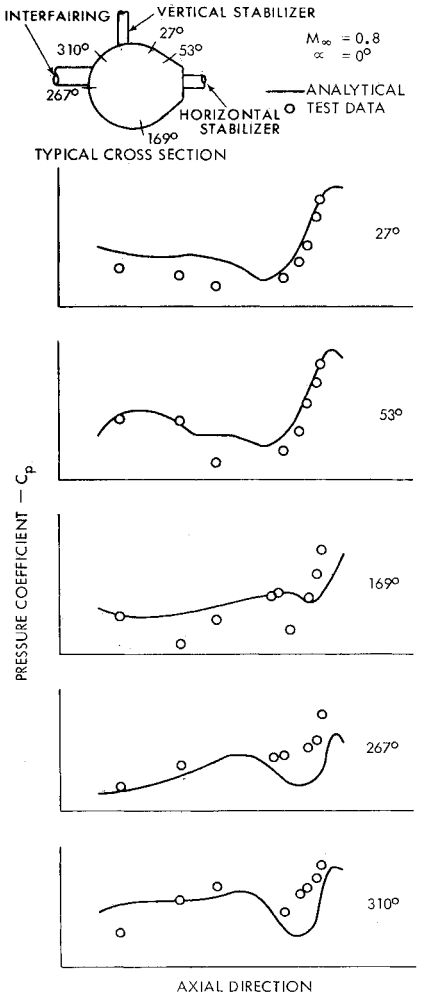


**Fig. 11 3-D aft end pressures.**

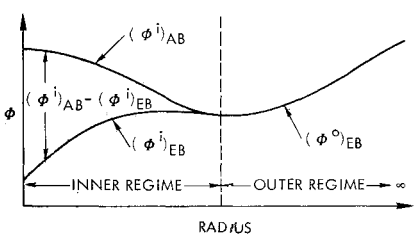


**Fig. 12 Flowfield regimes.**

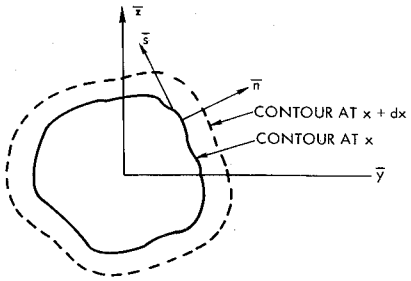


**Fig. 13 Surface coordinate system.**

To put this relation into a more lucid form, a coordinate system $n$ and $s$ normal and tangential to the contour surface is introduced as shown in Fig. 13.
Applying this coordinate transformation, Eq. (A6) becomes

$$\varphi_{2\bar{n}^i} = d\bar{n}/d\bar{s} \tag{A8}$$

where

$$d\bar{n} = (dB - B_{\bar{s}}d\bar{s})/B_{\bar{n}}$$

Equation (A8) states that the streamline slope must equal the surface slope in the plane normal to the $x$ axis. A solution of Eq. (A5) in terms of $r$ which satisfies Eq. (A8) may be obtained from Green's theorem[6]

$$\varphi_{2}{}^{i} = (1/2\pi)\oint(\varphi_{2\bar{n}^i} - \varphi_{2}{}^{i}\partial/\partial\bar{n})\ \ln\bar{r}_s d\bar{s}_s + g_2(x) \tag{A9}$$

In this relation

$$\bar{r}_s = [(\bar{y} - \bar{y}_s)^2 + (\bar{z} - \bar{z}_s)^2]^{1/2}$$

and the subscript $s$ identifies the location of the source of the body surface. For large $r$

$$(\partial/\partial\bar{n})(\ln\bar{r}_s)$$

may be neglected compared to $\ln\bar{r}_s$, and furthermore, $\bar{r}_s$ may be approximated by $\bar{r}$. Hence, the third term of the inner solution in its outer limit becomes

$$\epsilon^2\varphi_{2}{}^{i0} \sim [(1/2\pi)\ \ln\bar{r}\oint\varphi_{2\bar{n}^i}d\bar{s} + g_2(x)]\epsilon^2 \tag{A10}$$

Using Eq. (A8) and the relation

$$\oint(d\bar{n}/dx)d\bar{s}_1 = d\bar{S}/dx \tag{A11}$$

where

$$\bar{S}(x) = (1/\epsilon^2)S(x)$$

Equation (A10) becomes

$$\epsilon^2\varphi_{2}{}^{i0} \sim \{[\bar{S}'(x)/2\pi]\ \ln\bar{r} + g_2(x)\}\epsilon^2 \tag{A12}$$

The first term of Eq. (A12) is independent of Mach number and thus $g_2(x)$ must contain all the Mach number variations.

Remembering that $\varphi_1{}^i$ is a function of $x$ only, the cross-flow velocities for the outer limit of the inner-flow solution become (when substituting Eq. (A12) into (A4) and taking appropriate derivatives)

$$(U_y/U_\infty)\big|_{\bar{r}\to\infty} = (\partial\phi^i/\partial\bar{y})\big|_{\bar{r}\to\infty} = (\epsilon^2\bar{S}'(x)/4\pi r) + 0(\epsilon^3) \tag{A13}$$

$$(U_z/U_\infty)\big|_{\bar{r}\to\infty} = (\partial\phi^i/\partial\bar{z})\big|_{\bar{r}\to\infty} = (\epsilon^2\bar{S}'(x)/4\pi r) + 0(\epsilon^3) \tag{A14}$$

The transverse velocities for the outer flowfield become (using Eq. (A4)

$$U_y/U_\infty = \epsilon\varphi_{1y}{}^0 + \epsilon^2\varphi_{2y}{}^0 + 0(\epsilon^3) \tag{A15}$$

$$U_z/U_\infty = \epsilon\varphi_{1z}{}^0 + \epsilon^2\varphi_{2z}{}^0 + 0(\epsilon^3) \tag{A16}$$

Matching Eqs. (A13) and (A14) to (A15) and (A16), i.e.,

$$\phi^i\big|_{\substack{\bar{y}\to\infty\\ \bar{z}\to\infty}} = \phi^0\big|_{\substack{y\to 0\\ z\to 0}}$$

it is found that $\varphi_{1y}{}^0$ and $\varphi_{1z}{}^0$ must be zero. The only solution for $\varphi_1{}^0$ that will in addition satisfy the condition of vanishing perturbations at infinity is a constant which is taken as zero. Since $\varphi_1{}^0$ is zero, $\varphi_1{}^i$ must also be zero by matching. Thus, the outer limit of the inner-flow solution of Eq. (A1) for general slender bodies is

$$\phi^{i0} = U_\infty\{x + \epsilon^2[(\bar{S}'(x)/2\pi)\ \ln\bar{r} + g_2(x)]\} + 0(\epsilon^3) \tag{A17}$$

which is the same as the complete inner solution for an equivalent axisymmetric body having the same cross sectional area distribution.

The derivation shows that up to third order the inner-flow solution about a slender body approaches the inner flow solution about an equivalent body in the outer limit of the inner-flow regime. Since the same boundary conditions are satisfied (at the interface between the inner and outer-flow regimes and at infinity) as well as the same governing flow equations, the outer flow potential for an axisymmetric equivalent body and a general slender body must be identical. This fact is shown by the single line representing the outer potential in Fig. 12. The complete potential over a general slender body can therefore be represented as the sum of the potential over an equivalent body and the difference between the solutions of the two-dimensional Laplace equation, given by Eq. (A5) with two different body boundary conditions. This difference is given by the difference between Eq. (A9) and (A10). It is independent of Mach number because the term $g_2(x)$ in Eq. (A9) contains all the Mach number variations, is unaffected by the limit taken to obtain Eq. (A10), and thus drops out in the difference.

The velocity potential over an arbitrary slender body is therefore equal to the potential about the equivalent body plus a cross-flow potential which is independent of Mach number.

## References

[1] Spreiter, J. R. and Alksne, A. Y., "Slender Body Theory Based on Approximate Solution of the Transonic Flow Equation," TR R-2, 1959, NASA.

[2] Oswatitsch, K. and Keune, F., "The Flow Around Bodies of Revolution at Mach Number One," *Proceedings Conference on High Speed Aeronautics*, Polytechnic Institute of Brooklyn, 1955, pp. 113–131.

[3] Fink, M., "Calculated Transonic Flow Past Slender Fuselages and Afterbodies," *Journal of Aircraft*, Vol. 8, No. 9, Sept. 1971, pp. 710–716.

[4] Reshotko, E. and Tucker, M., "Approximate Calculation of the Compressible Turbulent Boundary Layer with Heat Transfer and Arbitrary Pressure Gradients," TN 4154, 1957, NACA.

[5] Van Dyke, M., *Perturbation Methods in Fluid Mechanics*, Academic Press, New York, 1964.

[6] Ashley, H. and Landahl, M., *Aerodynamics of Wings and Bodies*, Addison Wesley, Reading, Mass., 1965.